PHYSICAL REVIEW A **101**, 063404 (2020)

Hybrid Gaussian–discrete-variable representation for describing molecular double-ionization events

F. L. Yip,[1] C. W. McCurdy,[2,3] and T. N. Rescigno[2]
[1]Department of Science and Mathematics, California State University Maritime Academy, Vallejo, California 94590, USA
[2]Chemical Sciences, Lawrence Berkeley National Laboratory, Berkeley, California 94720, USA
[3]Department of Chemistry, University of California, Davis, California 95616, USA

(Received 4 April 2020; accepted 26 May 2020; published 12 June 2020)

A hybrid method that combines Gaussian basis functions typically used in bound-state molecular electronic structure calculations with a grid-based discrete-variable representation with finite elements suitable for a general electronic continuum representation is used to fully describe the double ionization of molecular H_2 by a single photoabsorption. This work expands the hybrid method, previously applied to single-ionization events, to double photoionization. Constructing the full two-electron operator encoding the electron correlation necessary to doubly ionize the target via the action of a single photon requires all classes of mixed integrals between combinations of the different basis-function types. Comparison of the present results with benchmark theoretical calculations and experimental results shows excellent agreement for both molecular H_2 and its united-atom limit, atomic helium; the triply differential cross sections that relate the angular distribution and energy sharing of all of the particles in the frame of the molecule are compared. The two-electron results computed using this hybrid basis hint at application of this general descriptive scheme beyond this simplest molecular target towards describing double ionization in more complicated and experimentally relevant molecules.

DOI: 10.1103/PhysRevA.101.063404

I. INTRODUCTION

The design and application of suitable and efficient representations for continuum processes, especially for a general molecular target, remain a continued goal for computational studies of collisional phenomena. In particular, double photoionization in which an atom or molecule yields two ejected electrons via the absorption of a single photon provides a direct pathway to observe the correlated electron dynamics since the process is driven by electron correlation [1–8]. For even the simplest molecular target, H_2, a full description of this process which can elucidate differential quantities such as energy sharing probabilities and angular distributions relative to the molecular axis (i.e., body-frame observations) requires sophisticated and computationally intensive treatments. This is due to the relatively small magnitude of the double-ionization amplitudes compared to the single-ionization channels that dominate at photon energies near the double-ionization threshold, wherein these small-probability events directly probe the electron correlation throughout the process [9]. In a similar vein, detailed experimental measurements that catch several ionized fragments in coincidence and can reconstruct the body-frame information at the moment of photoabsorption from the resulting momentum of the fragments represent the state of the art in fully describing such molecular processes where two electrons are ejected, followed by a Coulomb explosion of the residual target.

The fundamental molecule to investigate the detailed photoelectron angular distributions in the body frame from single-photon double ionization that has the most complete experimental measurements is H_2 (or D_2) [10–17]. Numerous *ab initio* theoretical calculations over the last few years have helped elucidate and inform these coincidence experiments [18–28]. Still, one of the challenges inherent in a theoretical description is the ability to accurately represent the molecular continuum states for even the simplest molecules like H_2. For example, pure grid-based calculations have dominated due to their computational advantages in producing highly structured multiprocessor representations of the operators and wave functions in a Born-Oppenheimer picture of molecular hydrogen that promotes the ground-state wave packet vertically into the electronic double continuum. For diatomic molecules such as H_2, another computational advantage can be gained by utilizing prolate-spheroidal coordinate systems that preserve the cylindrical symmetry of diatomics and build in the singularities at the foci and accurately represent cusps in the electronic wave function at the nuclei [26–28].

We previously reported an approach that treats the electronic coordinates using a combined representation with analytic Gaussian-type basis functions near the nuclei and overlapping a finite-element discrete-variable representation (FEM-DVR) grid-based approach that spans the radial coordinate into long-range regions that become relevant in ionization problems and must be able to efficiently represent the oscillatory nature of the continuum electrons far from the nuclei. In Refs. [29,30] (hereafter referred to as paper I and paper II, respectively), we described this "hybrid Gaussian basis" and applied it to molecular single photoionization. Subsequently, we also utilized this combined Gaussian-DVR representation to compute molecular-frame photoelectron angular distributions from heavier-nucleus diatomic molecules [31]. The underlying combination of analytical basis functions which are well suited and ubiquitous for computing exponentially decaying bound states in standard quantum chemistry calculations with grid-based FEM-DVR descriptions that provide efficient and essentially complete radial descriptions of unbounded states seeks to join the natural advantages of these different methods for describing molecular continuum processes, and these previous works have illustrated the application of these hybrid basis techniques to, so far, only single-photoionization processes. We note that, conceptually, the partitioning of the coordinate space into inner and outer regions has been utilized extensively in *R*-matrix theory for collisional physics [32], and the philosophical root with *R*-matrix theory that different regions of space can be treated uniquely is common to both approaches.

In this work, we extend the hybrid-basis methods to the substantially more challenging problem of double photoionization of two-electron targets. In particular, we describe and compute all of the specific classes of mixed two-electron integrals (i.e., unique combinations of Gaussian-type and FEM-DVR basis functions) and utilize all classes for the full two-electron problem. We previously enumerated these classes in paper II but have had occasion to utilize only certain classes for computing one-electron closed-shell direct and exchange operators in those previous molecular single-ionization studies [31]; here we shall need all of them. Additionally, we will incorporate the single-ionization continuum states represented in the hybrid Gaussian-DVR basis (which was primarily described in paper I) in order to extract the double-ionization amplitudes from all other energetically open processes using a computationally efficient testing-function formalism that we employed previously for similar double-ionization descriptions [23,33], including time-dependent implementations for representing few-photon absorptions [34]. The one-electron continuum functions are meant to be constructed using the hybrid basis in a manner similar to the full two-electron solution in order to extract the single-ionization continuum from the double-ionization components via orthogonality since both represent eigenstates of the same residual Hamiltonian.

In Sec. II, we overview the Gaussian-DVR method and enumerate the six particular classes of two-electron integrals that must be accurately represented in order to fully incorporate the electron-electron repulsion that drives the double-photoionization process. In order to provide a simpler case that is uncomplicated by the molecular geometry but still requires the (otherwise similarly constructed) electron-electron repulsion to be correctly represented, we first consider in Sec. III application of the hybrid basis to describe double ionization of atomic helium. This is followed by a brief comparison of results calculated for H_2 double ionization with a few key theoretical [21] and experimental benchmarks [13,16]. We conclude with brief remarks in Sec. IV.

II. THEORY

We begin with a brief summary of the key features of the hybrid Gaussian-DVR description of the electronic coordinates that will be employed in the double-ionization problems considered below. Further details of the method, particularly the construction of one-electron operators and application to single-ionization problems, can be found in papers I and II [29,30]. Atomic units are used throughout the following.

Figure 1 illustrates the main concepts of the hybrid Gaussian-DVR representation. From the origin (either at the nucleus of an atomic problem or at the midpoint of the internuclear distance for H_2) the radial coordinates of each electron will be subdivided into regions as shown in the top panel of Fig. 1. The innermost region constitutes the part of physical space that is purely described by Gaussian-type orbitals $G_i(\mathbf{r})$. Any standard quantum chemistry package that permits output of the relevant parameters (e.g., orbital exponents, normalization coefficients, etc.) and matrix elements between the Gaussian orbitals will suffice. Beyond this Gaussian region containing the nuclei of the target begins (at a radial distance r_0) a region described by both Gaussians $G_i(\mathbf{r})$ and FEM-DVR functions $\phi_j(r)$ in the radial coordinate with spherical harmonics encoding the angular coordinates,

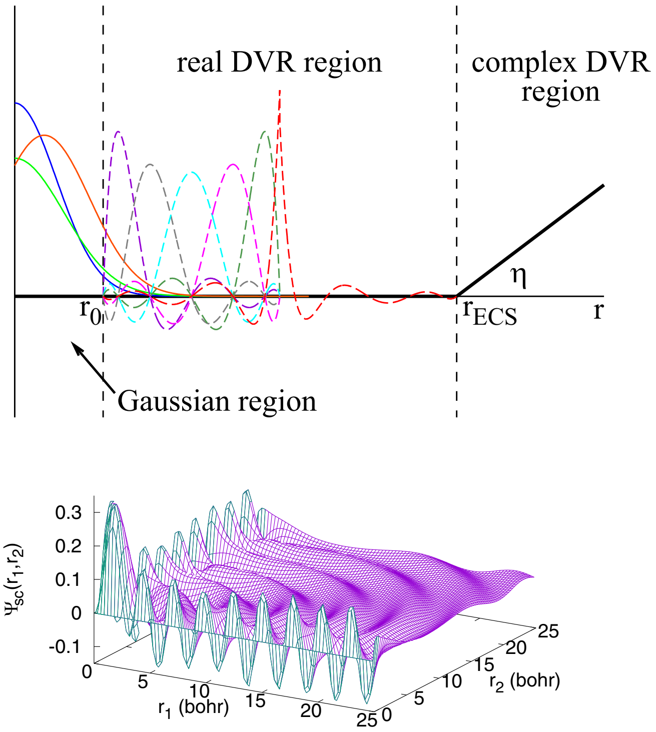

FIG. 1. Top: schematic of the radial coordinate partitioning in a hybrid Gaussian-DVR scheme. Inside of r_0 lie the nuclei of a molecular target, and Gaussian-type orbitals (GTOs) are used to describe the electronic coordinates. Beyond this region lie real FEM-DVR functions that overlap and connect with the Gaussian functions that decay exponentially well before the exterior complex scaling (ECS) rotation point. Only FEM-DVR functions exist in this complex-scaled region, which imposes the boundary conditions to produce outgoing-wave solutions. Bottom: The two leading components $[ks(1)kp(2) + kp(1)ks(2)]$ of the full-solution wave function (real part) plotted in the radial (r_1, r_2) plane. The colors highlight the partitioning of the radial space, with green indicating the portion of the wave function expanded only in GTOs (where either r_1 or r_2 is small, here within 1.0 bohr of each radial axis), while purple shows the overlap region where the full solution is expanded in both GTOs and FEM-DVR functions.

$$\chi_j^a(\mathbf{r}) = r^{-1}\phi_j(r)Y_{l^a,m^a}(\hat{\mathbf{r}}), \qquad (1)$$

which overlap with the exponentially decaying tails of the Gaussian functions centered only within the region bound by radius r_0. It is in this second region that the two different basis function formats overlap and connect to each other. In particular, the finite-element nature of the FEM-DVR permits flexibility in guaranteeing that the two portions of the overall basis are sufficiently connected while simultaneously seeking to avoid linear dependence. Aside from joining with the inner region via this overlap with the Gaussians, the FEM-DVR functions extend this intermediate region substantially further out towards a boundary where exterior complex scaling (ECS) rotates the radial coordinates of the ejected electrons into the complex plane and effectively allows the problem to be treated on a finite grid by imposing outgoing wave boundary conditions [33]. We note that this approach utilizes a single FEM-DVR grid primarily to provide the long-range description of the electron dynamics and is philosophically different from recent multicenter approaches that feature subgrids of FEM-DVR functions at different atomic centers [35], here instead using the Gaussian functions centered at each atom within the inner region to connect to the overall FEM-DVR grid.

The bottom panel of Fig. 1 shows the sum of the real part of the wave function for the two most dominant partial-wave terms within the full scattered solution $[ks(1)kp(2) + kp(1)ks(2)]$ of double photoionization of He plotted in the r_1, r_2 plane to illustrate the division of radial space in the hybrid method. The two colors differentiate where the inner region (lying close to either radial axis) is expanded only in Gaussian basis functions and where the FEM-DVR functions begin (typically less than an atomic length unit a_0 from the nearest nuclei). In practice, the connection between the different types of basis functions is limited to a few bohr distances from either axis (i.e., where the large peaks occur at small radial distances of either electron); this is also where the contributions to the double-ionization wave function are dominated by components at the total energy $E = (k_1^2 + k_2^2)/2$ that are particularly sensitive to the single-ionization channels open at the same total energy. This transition from primarily Gaussian basis functions to FEM-DVR functions occurs rather suddenly and obviates the need for diffuse Gaussian functions in favor of the FEM-DVR functions that will encode the smaller-amplitude double-ionization component, represented by the oscillatory fronts moving along the diagonal directions where both r_1 and r_2 increase.

A. Two-electron integrals in the hybrid Gaussian-DVR basis

We turn our focus now to the possible permutations of two-electron integrals that must be computed to fully describe the electron repulsion term $1/r_{12} = 1/|\mathbf{r}_1 - \mathbf{r}_2|$ that drives the single-photon double-ionization process in both atomic and molecular targets. There are six distinct permutations requiring a computational strategy that we enumerate as classes:

Class 1: $\langle G_i(\mathbf{r}_1)G_j(\mathbf{r}_2)|G_k(\mathbf{r}_1)G_l(\mathbf{r}_2)\rangle$,
Class 2: $\langle G_i(\mathbf{r}_1)G_j(\mathbf{r}_2)|G_k(\mathbf{r}_1)\chi_l^d(\mathbf{r}_2)\rangle$,
Class 3: $\langle G_i(\mathbf{r}_1)\chi_j^b(\mathbf{r}_2)|G_k(\mathbf{r}_1)\chi_l^d(\mathbf{r}_2)\rangle$,
Class 4: $\langle G_i(\mathbf{r}_1)G_j(\mathbf{r}_2)|\chi_k^c(\mathbf{r}_1)\chi_l^d(\mathbf{r}_2)\rangle$,
Class 5: $\langle G_i(\mathbf{r}_1)\chi_j^b(\mathbf{r}_2)|\chi_k^c(\mathbf{r}_1)\chi_l^d(\mathbf{r}_2)\rangle$,
Class 6: $\langle \chi_i^a(\mathbf{r}_1)\chi_j^b(\mathbf{r}_2)|\chi_k^c(\mathbf{r}_1)\chi_l^d(\mathbf{r}_2)\rangle$.

We utilize the indices i, j, k, and l above to label three-dimensional Gaussian-type orbitals and the radial FEM-DVR functions $\chi(r)$ of the grid-based functions, while labels a, b, c, and d index the angular coordinates of the latter [the spherical harmonics in Eq. (1)]. Both class-1 and class-6 integrals involve only a single type of basis function: either purely Gaussian or purely FEM-DVR functions. Class-1 integrals can be computed analytically by standard quantum chemistry packages. We have also extensively reported on class-6 integrals, computed by solving Poisson's equation at each discrete r_1, r_2 grid point and refer to Ref. [33] for the full details. We note the class-6 formulation particularly informs the computation of the mixed integrals in class 4 and class 5 below.

In what follows, we will frequently utilize a local representation of the charge density of the second electron's repulsion with the first as

$$I_{k,l}(\mathbf{r}_1) \equiv \int G_k(\mathbf{r}_2)\frac{1}{r_{12}}G_l(\mathbf{r}_2)\, d\mathbf{r}_2\,. \tag{2}$$

We begin our discussion of the mixed integrals with class 2, which possesses a single FEM-DVR function and allows us to make use of the local repulsion density in Eq. (2) to compute this integral as

$$\begin{aligned}\langle G_iG_j|G_k\chi_l^d\rangle &= \int\left(\int G_i(\mathbf{r}_1)\frac{1}{r_{12}}G_k(\mathbf{r}_1)\, d\mathbf{r}_1\right)\\ &\quad\times G_j(\mathbf{r}_2)\chi_l^d(\mathbf{r}_2)\, d\mathbf{r}_2\\ &= \int I_{i,k}(\mathbf{r}_2)G_j(\mathbf{r}_2)\frac{\phi_l(r_2)}{r_2}Y_{\ell^d,m^d}(\hat{\mathbf{r}}_2)\, d\mathbf{r}_2\\ &= r_l\sqrt{w_l}\int I_{i,k}(r_l;\hat{\mathbf{r}}_2)G_j(r_l;\hat{\mathbf{r}}_2)Y_{\ell^d,m^d}(\hat{\mathbf{r}}_2)\, d\hat{\mathbf{r}}_2,\end{aligned} \tag{3}$$

where the last line represents an angular integration [36] along a sphere at the radial distance of the FEM-DVR grid point r_l, as given by the underlying Lobatto quadrature of the FEM-DVR basis function definition [37].

The class-3 integrals are distinguished by having two Gaussian functions of the two-electron integral, both representing the coordinates of the same electron,

$$\begin{aligned}\langle G_i\chi_j^b|G_k\chi_l^d\rangle &= \int\left(\int G_i(\mathbf{r}_1)\frac{1}{r_{12}}G_k(\mathbf{r}_1)\, d\mathbf{r}_1\right)\\ &\quad\times \chi_j^{b*}(\mathbf{r}_2)\chi_l^d(\mathbf{r}_2)\, d\mathbf{r}_2\\ &= \int I_{i,k}(\mathbf{r}_2)\chi_j^{b*}(\mathbf{r}_2)\chi_l^d(\mathbf{r}_2)\, d\mathbf{r}_2,\end{aligned} \tag{4}$$

which becomes a diagonal matrix element in the radial coordinate of electron 2 when integrated using the underlying Lobatto quadrature of the FEM-DVR coordinates, yielding

$$\begin{aligned}\langle G_i\chi_j^b|G_k\chi_l^d\rangle &= \int I_{i,k}(\mathbf{r}_2)\frac{\phi_j(r_2)}{r_2}Y^*_{\ell^b,m^b}(\hat{\mathbf{r}}_2)\\ &\quad\times\frac{\phi_l(r_2)}{r_2}Y_{\ell^d,m^d}(\hat{\mathbf{r}}_2)\, d\mathbf{r}_2\\ &= \delta_{j,l}\int I_{i,k}(r_j;\hat{\mathbf{r}}_2)Y^*_{\ell^b,m^b}(\hat{\mathbf{r}}_2)Y_{\ell^d,m^d}(\hat{\mathbf{r}}_2)\, d\hat{\mathbf{r}}_2.\end{aligned} \tag{5}$$

The class-4 integrals are those that have a "mixed-exchange" nature of a Gaussian and an FEM-DVR for each of the two electrons and cannot be accurately represented simply by using Lobatto quadrature. Instead, we follow the re-expansion of the density of these mixed integrals, paralleling the computation of the pure FEM-DVR two-electron integrals [33]. The strategy is to utilize a multipole expansion for the electron repulsion,

$$\frac{1}{|\mathbf{r}_1-\mathbf{r}_2|}=\sum_{\lambda,\mu}\frac{4\pi}{2\lambda+1}Y_{\lambda,\mu}(\hat{\mathbf{r}}_1)\frac{r_<^{\lambda}}{r_>^{\lambda+1}}Y^*_{\lambda,\mu}(\hat{\mathbf{r}}_2), \tag{6}$$

along with a single-center expansion to represent the mixed Gaussian-DVR density,

$$rG_i(\mathbf{r})Y_{l',m'}(\hat{\mathbf{r}})=\sum_{l,m}R^{i,l',m'}_{l,m}(r)Y_{l,m}(\hat{\mathbf{r}}), \tag{7}$$

where the expansion coefficients are given by

$$R^{i,l',m'}_{l,m}(r)=r\int G_i(\hat{\mathbf{r}};r)Y_{l',m'}(\hat{\mathbf{r}})Y^*_{l,m}(\hat{\mathbf{r}})\,d\hat{\mathbf{r}}. \tag{8}$$

With these expansions, the mixed Gaussian-DVR integrals become

$$\begin{aligned}\langle G_iG_j|\chi_k^c\chi_l^d\rangle=&\sum_{\lambda,\mu}\frac{4\pi}{2\lambda+1}\iint\left[\sum_{l_1,m_1}R^{i,\ell^c,m^c}_{l_1,m_1}(r_1)(-1)^{m_1}Y^*_{l_1,-m_1}(\hat{\mathbf{r}}_1)\right]\phi_k(r_1)Y_{\lambda,\mu}(\hat{\mathbf{r}}_1)\frac{r_<^{\lambda}}{r_>^{\lambda+1}}Y^*_{\lambda,\mu}(\hat{\mathbf{r}}_2)\\&\times\left[\sum_{l_2,m_2}R^{j,\ell^d,m^d}_{l_2,m_2}(r_2)Y_{l_2,m_2}(\hat{\mathbf{r}}_2)\right]\phi_l(r_2)\,dr_1\,d\hat{\mathbf{r}}_1\,dr_2\,d\hat{\mathbf{r}}_2,\end{aligned} \tag{9}$$

which can be simplified using the orthonormality of the spherical harmonics to yield

$$\begin{aligned}\langle G_iG_j|\chi_k^c\chi_l^d\rangle=&\sum_{\lambda,\mu}\frac{4\pi}{2\lambda+1}\sum_{l_1,m_1}\sum_{l_2,m_2}\delta_{l_1,\lambda}\delta_{-m_1,\mu}\delta_{l_2,\lambda}\delta_{m_2,\mu}\left[(-1)^{m_1}\int R^{i,\ell^c,m^c}_{l_1,m_1}(r_1)\phi_k(r_1)\frac{r_<^{\lambda}}{r_>^{\lambda+1}}R^{j,\ell^d,m^d}_{l_2,m_2}(r_2)\phi_l(r_2)\,dr_1\,dr_2\right]\\=&\sum_{\lambda,\mu}\frac{4\pi(-1)^{\mu}}{2\lambda+1}\int R^{i,\ell^c,m^c}_{\lambda,-\mu}(r_1)\phi_k(r_1)\frac{r_<^{\lambda}}{r_>^{\lambda+1}}R^{j,\ell^d,m^d}_{\lambda,\mu}(r_2)\phi_l(r_2)\,dr_1\,dr_2.\end{aligned} \tag{10}$$

To evaluate the remaining integrations, we will use the radial density formalism

$$\int R^{i,\ell^c,m^c}_{l_1,m_1}(r_1)\phi_k(r_1)\frac{r_<^{\lambda}}{r_>^{\lambda+1}}R^{j,\ell^d,m^d}_{l_2,m_2}(r_2)\phi_l(r_2)\,dr_1\,dr_2=\left\langle\rho_1\left|\frac{r_<^{\lambda}}{r_>^{\lambda+1}}\right|\rho_2\right\rangle \tag{11}$$

to recast the integral as a solution of Poisson's equation that is reexpanded in the underlying radial basis. Using the mixed-basis two-electron density with the boundary conditions of the FEM-DVR basis $[r_0, r_{\max}]$ and specifying the surface terms yield the final result

$$\begin{aligned}\left\langle\rho_1\left|\frac{r_<^{\lambda}}{r_>^{\lambda+1}}\right|\rho_2\right\rangle=&(2\lambda+1)\left[\frac{R^{i,\ell^c,m^c}_{\lambda,-\mu}(r_k)}{r_k}\frac{R^{j,\ell^d,m^d}_{\lambda,\mu}(r_l)}{r_l}\right]\left[T^{\lambda}_{k,l}\right]^{-1}+\left(\frac{r_0^{2\lambda+1}-r_l^{2\lambda+1}}{r_0^{2\lambda+1}-r_{\max}^{2\lambda+1}}\right)\frac{R^{i,\ell^c,m^c}_{\lambda,-\mu}(r_k)R^{j,\ell^d,m^d}_{\lambda,\mu}(r_l)\sqrt{w_kw_l}\,r_k^{\lambda}}{r_l^{\lambda+1}}\\&+\left(\frac{r_l^{2\lambda+1}-r_{\max}^{2\lambda+1}}{r_0^{2\lambda+1}-r_{\max}^{2\lambda+1}}\right)\frac{R^{i,\ell^c,m^c}_{\lambda,-\mu}(r_k)R^{j,\ell^d,m^d}_{\lambda,\mu}(r_l)\sqrt{w_kw_l}\,r_0^{2\lambda+1}}{(r_kr_l)^{\lambda+1}},\end{aligned} \tag{12}$$

where $[T^{\lambda}_{i,l}]^{-1}$ is the inverse of the radial kinetic-energy matrix and w_k and w_l are the associated Lobatto quadrature weights for FEM-DVR points r_k and r_l, respectively [37]. Although computationally demanding, these class-4 matrix elements between mixed Gaussian and DVR functions (and those of the previous classes) need only be considered for finite elements possessing the nonzero range of the Gaussian functions, which lacks rather diffuse functions since the FEM-DVR functions provide primary coverage of the regions beyond the nuclei.

The class-5 integrals are those that have a single Gaussian-type function taken with three FEM-DVR basis functions. The strategy for their computation mirrors the multipole expansion of the class-4 integrals but is simplified due to the diagonal nature of the radial electronic coordinate for electron 2,

$$\begin{aligned}\langle G_i\chi_j^b|\chi_k^c\chi_l^d\rangle=&\sum_{\lambda,\mu}\left[\frac{4\pi}{2\lambda+1}\int G_i(\mathbf{r}_1)\phi_k(r_1)Y_{\ell^c,m^c}(\hat{\mathbf{r}}_1)Y_{\lambda,\mu}(\hat{\mathbf{r}}_1)\left(\int\phi_j(r_2)\phi_l(r_2)\frac{r_<^{\lambda}}{r_>^{\lambda+1}}Y_{\ell^d,m^d}(\hat{\mathbf{r}}_2)Y^*_{\ell^b,m^b}(\hat{\mathbf{r}}_2)Y^*_{\lambda,\mu}(\hat{\mathbf{r}}_2)\,d\mathbf{r}_2\right)d\hat{\mathbf{r}}_1\right]\\=&\sum_{\lambda,\mu}\left(\frac{4\pi}{2\lambda+1}\int G_i(r_k;\hat{\mathbf{r}}_1)Y_{\ell^c,m^c}(\hat{\mathbf{r}}_1)Y_{\lambda,\mu}(\hat{\mathbf{r}}_1)C(\ell^dm^d|\ell^bm^b,\lambda\mu)U^{\lambda}_{j,l}(r_k)\,d\hat{\mathbf{r}}_1\right).\end{aligned} \tag{13}$$

The angular integration of the second electron reduces to a Gaunt coefficient $C(jm|j'm',\lambda\mu)$, expressible in terms of the perhaps more familiar three-j symbol as [38]

$$C(jm|j'm',\lambda\mu)=\int Y_{j,m}(\hat{\mathbf{r}})\,Y^*_{j',m'}(\hat{\mathbf{r}})\,Y^*_{\lambda,\mu}(\hat{\mathbf{r}})\,d\Omega=(-1)^{m'+\mu}\sqrt{\frac{(2j+1)(2j'+1)(2\lambda+1)}{4\pi}}\begin{pmatrix} j & j' & \lambda \\ 0 & 0 & 0\end{pmatrix}\begin{pmatrix} j & j' & \lambda \\ m & -m' & -\mu\end{pmatrix}, \tag{14}$$

leaving an integral along the shell of electron 1, where

$$U^{\lambda}_{j,l}(r_k)=\int \phi_j(r_2)\phi_l(r_2)\frac{r_<^{\lambda}}{r_>^{\lambda+1}}\,dr_2=\delta_{j,l}\left[\frac{(2\lambda+1)}{r_k r_j\sqrt{w_k w_j}}\left[T^{\lambda}_{k,j}\right]^{-1}+\left(\frac{r_0^{2\lambda+1}}{r_0^{2\lambda+1}-r_{\max}^{2\lambda+1}}\right)\left(\frac{r_k^{\lambda}}{r_j^{\lambda+1}}+\frac{r_j^{\lambda}}{r_k^{\lambda+1}}-\frac{r_k^{\lambda}r_j^{\lambda}}{r_0^{2\lambda+1}}-\frac{r_{\max}^{2\lambda+1}}{r_k^{\lambda+1}r_j^{\lambda+1}}\right)\right]. \tag{15}$$

The final result restricts the sum to running over nonzero Gaunt coefficients and includes quadrature integrations of the Gaussian basis function evaluated at the kth Lobatto point, as was done for class-2 and class-3 integrals:

$$\langle G_i\chi_j^b|\chi_k^c\chi_l^d\rangle=\sum_{\lambda=|\ell^b-\ell^d|}^{\ell^b+\ell^d}\frac{4\pi}{2\lambda+1}U^{\lambda}_{j,l}(r_k)\left[\sum_{\mu=-\lambda}^{\lambda}C(\ell^d m^d|\ell^b m^b,\lambda\mu)\left(\int G_i(r_k;\hat{\mathbf{r}}_1)Y_{\ell^c,m^c}(\hat{\mathbf{r}}_1)Y_{\lambda,\mu}(\hat{\mathbf{r}}_1)\,d\hat{\mathbf{r}}_1\right)\right]. \tag{16}$$

With the mixed integrals specified above, the full electron repulsion operator can be constructed for all combinations that are required in a product basis of each electron's coordinates represented by these hybrid Gaussian-DVR basis functions. We note that where complex conjugations are required if bra and ket labels are reversed, care must be taken to conjugate only the angular functions if the radial coordinates have been complex scaled. The Gaussian basis is defined to be purely real and appreciably overlaps only the real portion of the FEM-DVR radial profile (middle area in the top panel of Fig. 1).

B. Ionization of two electrons by a single photon

The electronic Hamiltonian to describe two electrons in the Born-Oppenheimer approximation is

$$H=T_1+V_{\text{nuc}}(\mathbf{r}_1)+T_2+V_{\text{nuc}}(\mathbf{r}_2)+\frac{1}{r_{12}}, \tag{17}$$

where $T+V_{\text{nuc}}=h$ is the one-electron Hamiltonian including the kinetic energy and nuclear attraction potential (either $V_{\text{nuc}}=-2/r$ in the case of atomic helium or $V_{\text{nuc}}=-1/|\mathbf{r}-R/2|-1/|\mathbf{r}+R/2|$ for the case of H_2 with a fixed internuclear distance R).

The double-ionization amplitudes can be computed from the full scattering solution with outgoing-wave boundary conditions that solves the first-order driven Schrödinger equation

$$[E_0+\hbar\omega-H]\Psi^+_{\text{sc}}(\mathbf{r}_1,\mathbf{r}_2)=\vec{\epsilon}\cdot(\vec{\mu}_1+\vec{\mu}_2)\varphi_0(\mathbf{r}_1,\mathbf{r}_2), \tag{18}$$

where $E=E_0+\hbar\omega$ is the total excess energy above the double-ionization potential E_0 available to the system after photoabsorption (in the dipole approximation) from the initial state $\varphi_0(\mathbf{r}_1,\mathbf{r}_2)$. The amplitudes for double-ionization ejecting electrons with momenta $\mathbf{k}_1$ and $\mathbf{k}_2$ can be evaluated as a volume integral

$$\begin{aligned}f(\mathbf{k}_1,\mathbf{k}_2)=&\langle\Phi^{(-)}(\mathbf{k}_1,\mathbf{r}_1)\Phi^{(-)}(\mathbf{k}_2,\mathbf{r}_2)|\\ &\times E-h(\mathbf{r}_1)-h(\mathbf{r}_2)|\Psi^+_{\text{sc}}(\mathbf{r}_1,\mathbf{r}_2)\rangle,\end{aligned} \tag{19}$$

where $\Phi^{(-)}(\mathbf{k},\mathbf{r})$ is the incoming continuum wave function related to the outgoing version by $\Phi^{(-)}(\mathbf{k},\mathbf{r})=[\Phi^{(+)}(-\mathbf{k},\mathbf{r})]^*$ that satisfies

$$\left[T+V_{\text{nuc}}-\frac{k^2}{2}\right]\Phi^{(+)}(\mathbf{k},\mathbf{r})=0. \tag{20}$$

In the case of atomic helium, $\Phi^{(+)}(\mathbf{k},\mathbf{r})$ is a Coulomb scattering solution constructed in a partial-wave expansion,

$$\Phi^{(+)}_c(\mathbf{k},\mathbf{r})=\left(\frac{2}{\pi}\right)^{1/2}\sum_{l,m}i^l e^{i\eta_l(k)}Y^*_{l,m}(\hat{\mathbf{k}})\frac{\phi^{(c)}_{l,k}(r)}{kr}, \tag{21}$$

using the hybrid Gaussian-DVR basis. For molecular H_2, $\Phi^{(-)}(\mathbf{k},\mathbf{r})$ is a continuum state of the residual molecular geometry, i.e., a scattering state of ${H_2}^+$,

$$\Phi^{(+)}(\mathbf{k},\mathbf{r})=\xi(\mathbf{k},\mathbf{r})+g(r)\Phi^{(+)}_c(\mathbf{k},\mathbf{r}), \tag{22}$$

which we have partitioned as the same atomic Coulomb wave in Eq. (21) plus a short-range correction, where $g(r)$ is an arbitrary smooth function that approaches unity at large r and cuts off the Coulomb function for smaller r. For both the atomic and molecular geometries, the radial Coulomb waves $\phi^{(c)}_{l,k}(r)$ behave asymptotically as $\sin[kr+(Z/k)\ln 2kr-\pi l/2+\eta_l(k)]$, with $Z=2$ and possessing Coulomb phase shift $\eta_l(k)=\arg\Gamma(l+1+iZ/k)$.

The short-range distortion $\xi(\mathbf{k},\mathbf{r})$ due to the nonsperhical molecular geometry in Eq. (22) is also to be expanded in the hybrid Gaussian-DVR basis for each incoming partial-wave channel l_0

$$\frac{\xi(\mathbf{r})^{l_0,m}}{r}=\sum_{\Gamma}c^{l_0,m}_{\Gamma}G_{\Gamma}(\mathbf{r})+\sum_{i,l}c^{l_0,m}_{il}\frac{\phi_i(r)}{r}Y_{l,m}(\hat{\mathbf{r}}), \tag{23}$$

where the index Γ labels the Gaussian basis functions coupled to l_0 and the cylindrical symmetry of either He or H_2 renders m a good quantum number. This partial-wave decomposition leads to a set of driven equations for each incoming l_0, m

Coulomb wave channel,

$$\left[\frac{k^2}{2} - (T + V_{\text{nuc}})\right]\frac{\xi^{l_0,m}(\mathbf{r})}{r} = \left[(T + V_{\text{nuc}}) - \frac{k^2}{2}\right] g(r)\frac{\phi^{(c)}_{l_0,k}(r)}{r} Y_{l_0,m}(\hat{\mathbf{r}}). \tag{24}$$

As we previously employed [21,33], the six-dimensional volume integral in Eq. (19) is operationally converted to a surface integral using Green's theorem along a constant hyperradius ρ_0 to give the double-ionization amplitudes,

$$\begin{aligned} f(\mathbf{k}_1, \mathbf{k}_2) = {} & \int d\Omega_1 \int d\Omega_1 \int d\rho \int_0^{\pi/2} d\alpha \frac{\rho^5 \sin^2\alpha \sin^2\alpha}{2} \\ & \times \Phi^{(-)}(\mathbf{k}_1, \mathbf{r}_1)^* \Phi^{(-)}(\mathbf{k}_2, \mathbf{r}_2)^* \\ & \times \left[\frac{\overleftarrow{\partial}}{\partial\rho}\delta(\rho - \rho_0) - \delta(\rho - \rho_0)\frac{\overrightarrow{\partial}}{\partial\rho}\right]\Psi^+_{\text{sc}}(\mathbf{r}_1, \mathbf{r}_2), \end{aligned} \tag{25}$$

where $\rho = \sqrt{r_1^2 + r_2^2}$ and $\tan\alpha = r_2/r_1$. Also, the arrows above the partial derivatives with respect to ρ indicate the direction they should operate, and the δ functions confine the integral to a particular hyperradius inside of the ECS scaling point r_{ECS}. This testing function formalism reduces to an integration of the quantity in Eq. (25) along a quarter-circle arc at sufficiently large ρ_0 in the r_1, r_2 plane (see the bottom panel of Fig. 1) and eliminates all energetically open contributions from the full solution $\Psi^+_{\text{sc}}(\mathbf{r}_1, \mathbf{r}_2)$ that are not double ionization by orthogonality; we previously utilized this method to compute double-ionization amplitudes provided the testing functions $\Phi^{(-)}(\mathbf{k}, \mathbf{r})$ are continuum solutions of the residual one-body Hamiltonian that appears in the correlated full Hamiltonian [Eq. (17)] [34,39–42].

III. RESULTS

In what follows we present a few results to compare with benchmark theory calculations and experimental measurements. The examples we present here are representative of some of the key features that were previously explored in double photoionization of He and H_2; they permit us to evaluate the accuracy of the hybrid Gaussian-DVR basis and highlight the advantages of the method, primarily requiring fewer partial-wave terms in the outer FEM-DVR region to yield accurate results compared to pure grid-based calculations by utilizing the Gaussian basis to describe the region of physical space containing the nuclei [31].

The most detailed information to be studied in a double-photoionization event is the fully differential cross section, given in the length gauge by

$$\frac{d\sigma}{dE_1 d\Omega_1 d\Omega_1} = \frac{4\pi^2\omega}{c} k_1 k_2 |f(\mathbf{k}_1, \mathbf{k}_2)|^2, \tag{26}$$

where, for what follows on molecular H_2 in the Born-Oppenheimer approximation, we have made the reasonable approximation that a transition via the photoabsorption occurs vertically at the equilibrium internuclear distance $R_{\text{eq}} = 1.4$ a.u. and the Coulomb explosion of the bare protons proceeds without deposition of significant energy from the photon. Observing these events in the molecular frame also requires consideration of the molecular geometry relative to the photon polarization direction, here taken to be linear and horizontal in the figures that follow. For H_2, this establishes three photoionization amplitudes: one of Σ_u symmetry and two equivalent Π_u contributions reflecting the possible final magnetic quantum states, $M = m_1 + m_2$, that can be populated by a linearly polarized photon from the $1\sigma_g^2$ ground state of H_2.

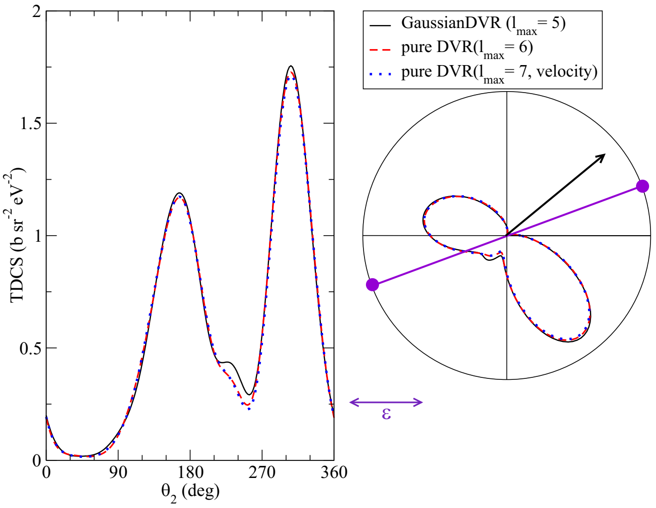

FIG. 2. Triple-differential cross section (TDCS) results for double photoionization of H_2 at a photon energy of 75 eV; the left panel shows the absolute cross section in the coplanar geometry; the right panel provides a polar plot of the same. Directions are measured relative to the linear polarization vector (horizontal in the right panel). The fixed electron (black arrow) is held at $\theta_1 = 40^\circ$, and the internuclear axis is at $\theta_N = 20^\circ$. For this case, the contributions of the relevant dipole-allowed amplitudes of Σ_u and Π_u symmetry contribute approximately equally. The present results calculated using the hybrid Gaussian-DVR basis (black solid line) agree well with the benchmark pure grid-based FEM-DVR results [23] for different angular momentum maximum values of each electron, $l_{\text{max}} = 6$ and $l_{\text{max}} = 7$ (red long-dashed and blue short-dashed lines, respectively).

It is noteworthy that for H_2 at the photon energy $\omega = 75$ eV considered here, the $M = \pm 1$ contributions are generally larger in magnitude than the $M = 0$ amplitudes and can often dominate the fully differential cross section. In our first example of the body-frame triple-differential cross section (TDCS) calculated using the hybrid Gaussian-DVR method for comparison with a pure grid-based calculation [21], we again choose a case where the Σ_u and Π_u amplitudes contribute roughly equally. Figure 2 shows the TDCS for a second electron ejected from an equilibrium geometry H_2 molecule rotated at an angle of $\theta_{\text{mol}} = 20^\circ$ relative to the polarization of the light with the first electron carrying 80% of the available excess energy and with a direction of $\theta_1 = 40^\circ$. The present results, calculated with an inner-region Gaussian basis consisting of 36 basis functions of s, p, and d angular momenta centered on the nuclei and at the molecular center, and FEM-DVR functions beginning at $r_0 = 0.8$ bohr containing up to $l_{\text{max}} = 5$ for each electron are compared to pure FEM-DVR calculations with up to $l_{\text{max}} = 6$ and $l_{\text{max}} = 7$. The latter pure

FEM-DVR calculation is also computed in the velocity gauge, while the hybrid results and smaller grid-based calculation are computed in the length gauge. Evaluation of the dipole terms in the hybrid basis is more straightforward in the length gauge, but we note that the results presented here agree well with both the length and velocity forms of the pure FEM-DVR calculations. These results illustrate very good agreement between the present results and the benchmark grid-based calculations (of both gauges), with the most visible differences arising in the valley between primary and secondary lobes around $\theta_2 \sim 220^\circ$, as well as the very slight differences in the peak heights. A comparison of these results reveals that the present representation of the bound and continuum states is fairly well converged to resolve the significant features and accurately compute the TDCS that results from incorporating the various polarization-dependent amplitudes.

A. Helium double photoionization at $\omega = 99$ eV

Because it is a well-studied problem [1–8] with many theoretical calculations and experimental measurements in good agreement while still providing a system for which the correlation introduced via the electron repulsion term (and thus the two-electron matrix elements of Sec. II A) must be accurately represented, we utilized the hybrid Gaussian-DVR basis to compute TDCS results for double photoionization of helium at a photon energy of 99 eV and present a few representative results. We note that this problem is the united-atom limit of the molecular H_2 double ionization, and thus, we can expect the $M = \pm 1$ amplitudes and $M = 0$ to become equivalent as the internuclear distance approaches zero and the target becomes spherically symmetric.

Figure 3 shows the coplanar geometry TDCS results for double ionization of helium with the fixed electron at $\theta_1 = 0^\circ$ along the polarization direction (top panels) and with $\theta_1 = 90^\circ$ relative to the polarization (bottom panels). These results were computed with an inner-region basis of 12 total Gaussian functions of types s and p centered at the origin. The s-type Gaussian exponents are those of the first six from Huzinaga's $10s$ expansion of the hydrogen $1s$ function in Gaussians [43], while those of the p-type orbitals have exponents of $\alpha = 2.0$ and 0.5. The FEM-DVR functions begin at a radius of $r_0 = 1.0$ bohr from the origin and use six real finite elements with a 15th-order DVR in each, up to the ECS scaling point of $r_{\mathrm{ECS}} = 45.0$ a.u. The region for evaluation of the mixed two-electron integrals over which the Gaussians are considered sufficiently nonzero extends up to $r = 15.0$ a.u. In the FEM-DVR region, all angular terms are computed with up to $l_{\max} = 3$ for each electron. The energy sharing of the excess energy delivered by the photon is split equally between the two electrons ($E_1 = E_2 = 10$ eV). Figure 4 shows the same coplanar geometry and equal energy sharing for helium, but now with the fixed electron going out in directions of $\theta_1 = 30^\circ$ and $\theta_1 = 60^\circ$, respectively. Again, the agreement between the present results calculated with the hybrid Gaussian-DVR basis and previous benchmark calculations [6–8] is excellent.

Included with the present results (black curves) in both Figs. 3 and 4 are results computed using a pure grid-based FEM-DVR calculation with similar numerical parameters (but beginning at the origin). Comparison of these results for the two calculations reveals excellent agreement in both magnitude and angular profile of the lobed structure, indicating an accurate representation of the electron-electron repulsion mixed integrals that properly encodes the physics that drives the double-ionization process. Both Figs. 3 and 4 also exhibit angular distributions influenced by a parity-selection rule which prevents both electrons from exiting in back-to-back directions with equal energy [44].

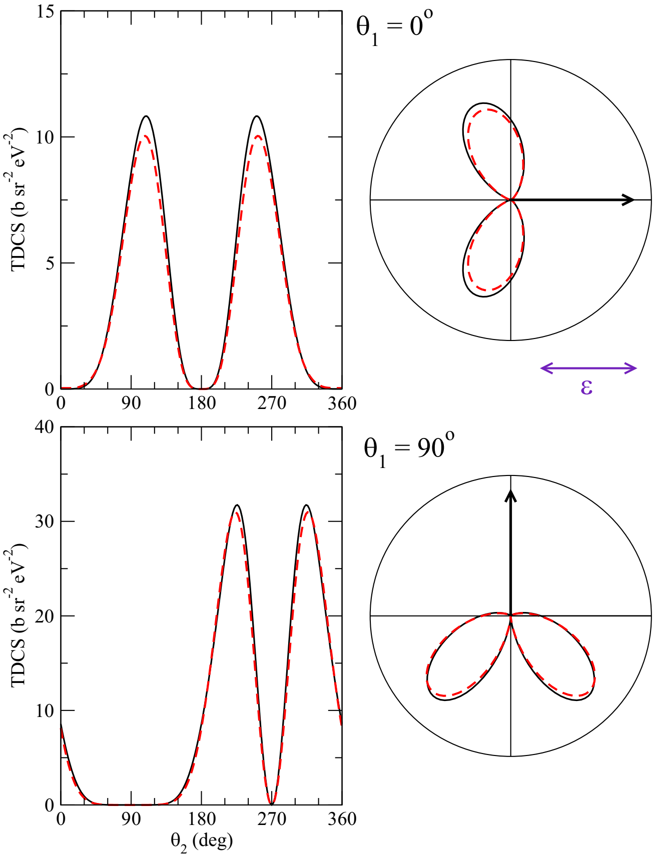

FIG. 3. Triple-differential cross section (TDCS) results for double photoionization of atomic helium at a photon energy of 99 eV with equal energy sharing ($E_1 = E_2$); the left panels show the absolute cross section in the coplanar geometry, and right panels show polar plots of the same. The fixed electron (black arrow) is held at $\theta_1 = 0^\circ$ (top panels) and at $\theta_1 = 90^\circ$ (bottom panels). Hybrid Gaussian-DVR results (solid black line) again agree well with benchmark FEM-DVR results (red dashed line). As one approaches this united-atom extreme, the Σ_u and Π_u amplitudes become equivalent.

B. H_2 double photoionization at $\omega = 75$ eV

Of course, the motivation for designing the hybrid Gaussian-DVR basis is not to treat spherical targets (as grid-based single-center expansions are well suited for atoms) but to treat molecular targets with off-center geometries. For H_2, we construct the inner-region basis by duplicating the hydrogen-atom basis from the united-atom limit above onto each hydrogen nuclei at an equilibrium internuclear distance of $R = 1.4$ bohr. The geometric center provides the origin of our coordinate system, with the internuclear axis marking the z direction in the body frame. In addition to this basis, d-type

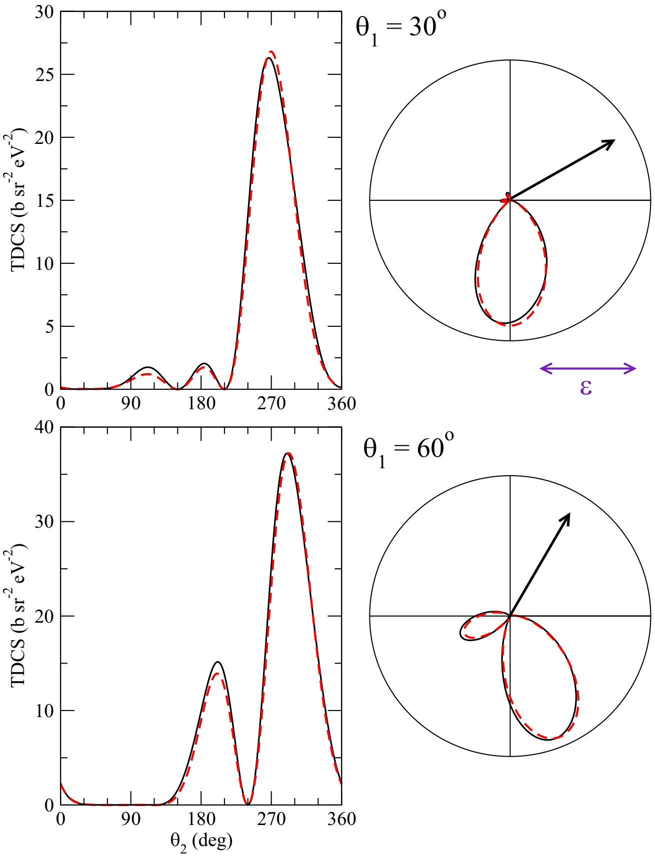

FIG. 4. Same as Fig. 3, but with the fixed electron (black arrow) held at $\theta_1 = 30^\circ$ (top panels) and at $\theta_1 = 60^\circ$ (bottom panels).

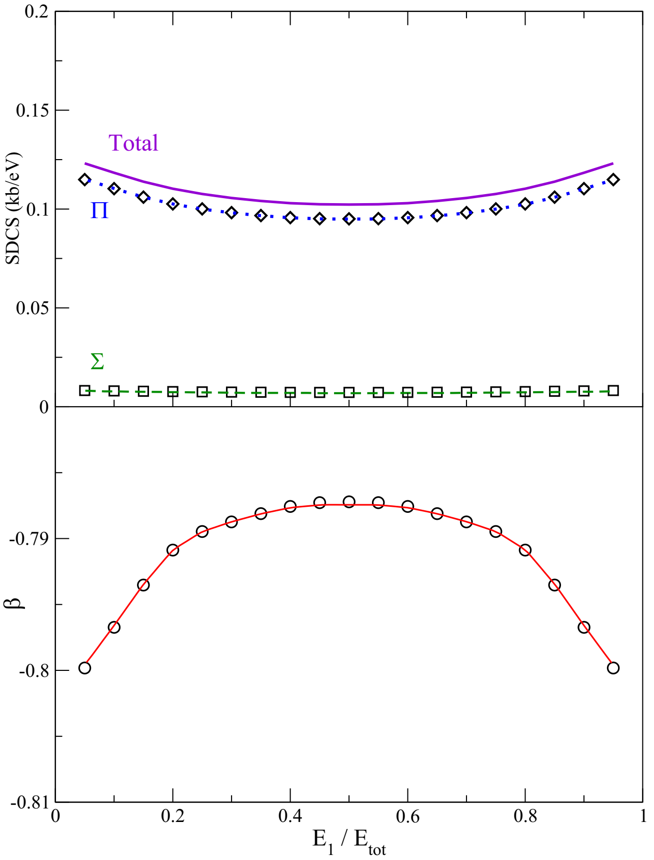

FIG. 5. Top: single-differential cross section (SDCS) results for double photoionization of equilibrium geometry H_2 at a photon energy of 75 eV by unique M components, Σ_u (dashed line) and Π_u (dotted line), as well as the total from the sum of these two contributions (solid line). Also shown are pure grid-based results (symbols), again showing nearly graphically indistinguishable agreement with the benchmark calculations. Bottom: molecular asymmetry parameter $\beta(E_1)$ as a function of the energy sharing. The present results agree substantially with the pure FEM-DVR results (circles).

Gaussian functions are added to each hydrogen atom center with exponent $\alpha = 0.75$, and to provide sufficient coverage of the internuclear region, we augmented this inner region with a few nondiffuse (i.e., smallest exponent $\alpha = 0.5$) s-, p-, and d-type Gaussian functions at the center of the molecule. The remaining radial FEM-DVR grid parameters are unchanged from those above, except for beginning the FEM-DVR region at $r_0 = 0.8$ bohr from the internuclear center and including angular terms containing up to $l_{\max} = 5$, which is less than the maximum single-electron angular momentum used to calculate converged pure FEM-DVR results for comparison ($l_{\max} = 7$). The starting point for the radial FEM-DVR grid excludes the nuclei from the overlap region, keeping them exclusively within the inner Gaussian region where higher partial-wave contributions at the nuclear cusps can be encoded in the Gaussian basis expansion.

We begin our examination of the hybrid basis results by considering double photoionization from H_2 at a photon energy of $\omega = 75$ eV. Integrating the body-frame TDCS given by Eq. (26) over the directions of the electrons gives the single-differential cross section (SDCS), which reflects the energy sharing of the ejected electrons carrying the (vertical) energy above the double-ionization potential. Both unique components of Σ_u and Π_u symmetry (reflecting the polarization direction relative to the molecular axis) are plotted in the top panel of Fig. 5, along with the total SDCS. We note that for the nonspherical molecular geometry, these distinct contributions are now substantially different in magnitude, whereas they are identical (accounting for the double degeneracy of Π_u) in the united-atom limit of the previous helium results. From these relative magnitudes, we anticipate that the amplitudes containing Π_u components will dominate those of the weaker Σ_u contributions for most molecular orientations that mix them. Also shown is the comparison with a pure FEM-DVR calculation [23], with $l_{\max} = 7$, for which the agreement is excellent.

The bottom panel of Fig. 5 shows the molecular asymmetry parameter $\beta(E_1)$, given by

$$\beta(E_1) = \frac{2\left(\frac{d\sigma^{(\Sigma)}}{dE_1} - \frac{d\sigma^{(\Pi)}}{dE_1}\right)}{\left(\frac{d\sigma^{(\Sigma)}}{dE_1} + 2\frac{d\sigma^{(\Pi)}}{dE_1}\right)}, \tag{27}$$

for different energy sharings of the available excess energy. Again, comparison of the present results is very good with the converged pure FEM-DVR grid-based calculation and with experimental results measured at equal-energy sharing: $\beta = -0.78$ in the present results compared with the value of $\beta = -0.75 \pm 0.1$ measured by Gisselbrecht *et al.* [16].

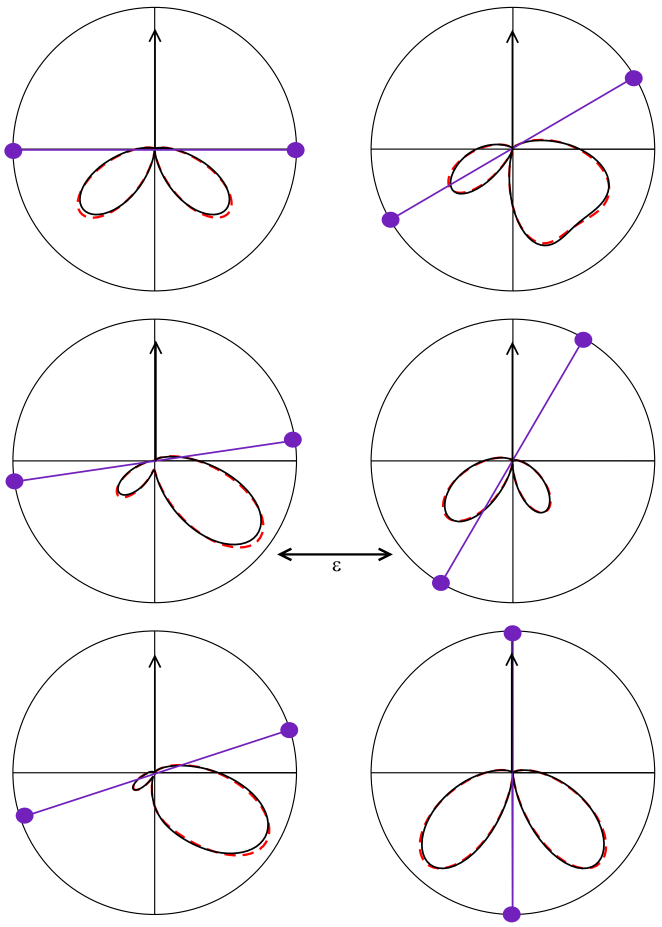

FIG. 6. Molecular-frame triple-differential cross section (TDCS) results for double photoionization of H_2 at a photon energy of 75 eV and with a fixed electron (black arrow) held at $\theta_1 = 90^\circ$ and carrying 20% of the available excess energy. Each panel shows a different molecular orientation relative to the linear polarization vector (horizontal): the left column has $\theta_N = 0^\circ$, 10°, and 20°; the right column has $\theta_N = 30^\circ$, 60°, and 90°. In all panels, the present hybrid Gaussian-DVR results (black solid lines) agree excellently with the pure FEM-DVR results (red dashed lines). These theoretical results are computed at the precise angles denoted and thus feature no averaging (see text).

To demonstrate the agreement of the hybrid-basis TDCS with converged benchmark calculations for a few representative results, Fig. 6 shows the in-plane TDCS for unequal energy sharing, with the fixed electron carrying 20% of the available excess energy and fixed in a direction perpendicular to the (horizontal) polarization direction. Each panel shows the angular distribution as the molecule is rotated relative to the polarization. The top left and bottom right panels show cases where the cross section contains only nonzero components from the Σ_u and Π_u continua, respectively. A comparison with the converged pure FEM-DVR results [23] reveals superb agreement. Examination of these TDCS reveals that for the geometries that involve only pure Σ_u and Π_u configurations, the dominant feature is two lobes directed away from the fixed electron with no significant cross section in the back-to-back direction that can be characterized as atomiclike in that they resemble the angular distribution from the similar geometry of the fixed electron perpendicular to the polarization direction (see bottom panel of the helium results in Fig. 3), although the Π_u cross section is several times the magnitude of the pure Σ_u cross section.

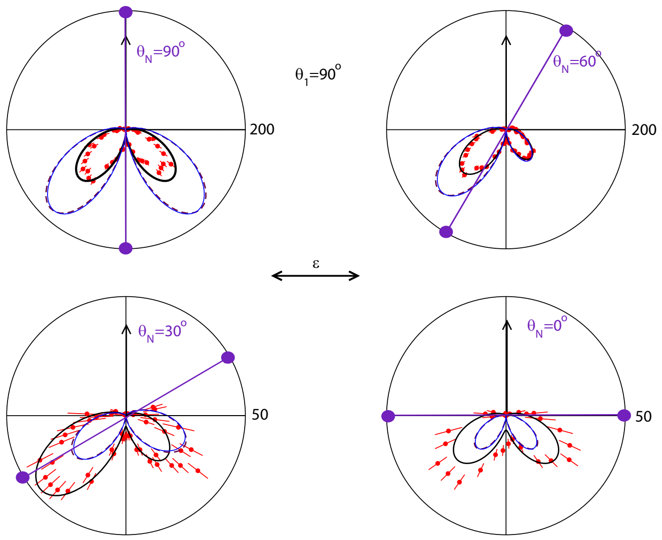

FIG. 7. Molecular-frame TDCS results for double photoionization of H_2 at a photon energy of 75 eV and with a fixed electron (black arrow) held at $\theta_1 = 90^\circ$ and carrying 50% of the available excess energy (equal energy sharing). Each panel shows a different molecular orientation relative to the linear polarization vector (horizontal), as indicated: unaveraged theoretical results calculated with the hybrid Gaussian-DVR basis (thin blue line) and with the pure FEM-DVR treatment (dashed violet line) again show good agreement with each other. Comparison with the experimental measurements (red circles) of Ref. [16] requires an averaging of the hybrid results over the experimentally determined acceptance angles (thick black lines; see text). Magnitudes of the cross sections (in b eV^{-1} sr^{-2}) are shown in each panel denoting the radii of each polar plot.

Because of this discrepancy between the magnitudes of the Σ_u and Π_u contributions, it is noteworthy that when compared with experimental measurements where finite angular resolution must be accounted for, the theoretical results for measuring the body-frame position relative to the polarization must also be averaged over a range of acceptance angles. This is particularly most sensitive for measurements that would seemingly probe the Σ_u amplitudes since including other molecular geometries that move the body-frame z axis away from the polarization quickly introduces substantial contributions from Π_u that can swamp the $M = 0$ components. In Fig. 7, we provide a comparison of the theoretical TDCS calculated with the hybrid Gaussian-DVR basis and a pure FEM-DVR calculation and also with experimental results [16] at equal energy sharing ($E_1 = E_2$). The averaging angles for this in-plane geometry with the fixed electron perpendicular to the photon polarization are those of Ref. [16]: $\Delta\theta_1 = \pm 15^\circ$ and $\Delta\theta_N = \pm 20^\circ$ in the first three panels and $\Delta\theta_1 = \pm 20^\circ$ and $\Delta\theta_N = \pm 30^\circ$ in the final (bottom right) panel. The thin lines represent the unaveraged calculations (including the benchmark results for Ref. [23]), while the thicker black line is the result of the present hybrid results averaged over the acceptance angles of the experiment. We can see the result of the averaging produces good agreement with the experimental results and substantially alters the magnitude of the major features of the unaveraged cross sections at all of the internuclear orientations considered.

IV. CONCLUSIONS

In this work, we have overviewed and applied a hybrid basis of Gaussian-type functions combined with grid-based methods to describe molecular double photoionization. The enumeration and strategy to evaluate each class of mixed two-electron integrals have been established to describe the double-ionization event which relies on the correlation being properly represented. Several results computed with this hybrid Gaussian method, both for atomic helium and for molecular H_2, and compared with benchmark theoretical calculations and experimental measurements reveal excellent agreement of the hybrid Gaussian-DVR results with the existing data. Atomic helium results help establish the accuracy of the electron-electron repulsion encoded in the present formulation, while the angle-resolved triple-differential and (single) energy-differential cross sections for H_2 at the equilibrium internuclear geometry highlight the richness of the results that are particularly sensitive to the molecular-frame environment.

Having established sufficient agreement with several key results for H_2, it is hoped that this hybrid Gaussian-DVR method can be used to treat other diatomic molecules and, eventually, polyatomic molecules where a pure grid-based single-center expansion might be difficult to converge. In particular, being able to sufficiently treat the ejection of two valence electrons by representing them in a hybrid basis in the presence of additional core electrons of the molecular target that would remain bound to the fragments is one avenue for exploration that we hope to further consider. Such a description of a multielectron molecule possessing the occupancy of core molecular orbitals constructed with Gaussian-type orbitals in the inner region would allow for an accounting of these core electrons' influence on the electrons that do become photoejected. Having utilized approximations to consider multielectron targets in atomic double ionization [39–42] and illustrated the hybrid basis's ability to construct closed-shell core and valence molecular orbitals for single ionization [31], the next step to consider is double ionization of a many-electron molecule with a frozen-core occupancy. The results presented here provide necessary confirmation of the hybrid Gaussian-DVR method for describing two electrons in the nontrivial molecular continuum and strongly hint at the utility of expanding this method for treating more complicated and experimentally relevant molecular targets in double-ionization studies.

ACKNOWLEDGMENTS

Work was performed at the University of California Lawrence Berkeley National Laboratory under Contract No. DE-AC02-05CH11231 and was supported by the US DOE Office of Basic Energy Sciences, Chemical Sciences, Geosciences, and Biosciences Division and by the US Department of Energy, Office of Science, Office of Workforce Development for Teachers and Scientists (WDTS) under the Visiting Faculty Program (VFP). F.L.Y. acknowledges support from the National Science Foundation, Award No. PHY-1806417.

---

[1] L. Avaldi and A. Huetz, J. Phys. B **38**, S861 (2005).
[2] R. Dörner, J. M. Feagin, C. L. Cocke, H. Bräuning, O. Jagutzki, M. Jung, E. P. Kanter, H. Khemliche, S. Kravis, V. Mergel *et al.*, Phys. Rev. Lett. **77**, 1024 (1996).
[3] R. Dörner, H. Bräuning, J. M. Feagin, V. Mergel, O. Jagutzki, L. Spielberger, T. Vogt, H. Khemliche, M. H. Prior, J. Ullrich *et al.*, Phys. Rev. A **57**, 1074 (1998).
[4] H. Bräuning, R. Dörner, C. L. Cocke, M. H. Prior, B. Krässig, A. S. Kheifets, I. Bray, A. Bräuning-Demian, K. Carnes, S. Dreuil *et al.*, J. Phys. B **31**, 5149 (1998).
[5] P. Bolognesi, V. Feyer, A. Kheifets, S. Turchini, T. Prosperi, N. Zema, and L. Avaldi, J. Phys. B **41**, 051003 (2008).
[6] P. Selles, L. Malegat, and A. K. Kazansky, Phys. Rev. A **65**, 032711 (2002).
[7] C. W. McCurdy, D. A. Horner, T. N. Rescigno, and F. Martín, Phys. Rev. A **69**, 032707 (2004).
[8] D. A. Horner, J. Colgan, F. Martín, C. W. McCurdy, M. S. Pindzola, and T. N. Rescigno, Phys. Rev. A **70**, 064701 (2004).
[9] R. Y. Bello, F. L. Yip, T. N. Rescigno, R. R. Lucchese, and C. W. McCurdy, Phys. Rev. A **99**, 013403 (2019).
[10] T. J. Reddish, J. P. Wightman, M. A. MacDonald, and S. Cvejanović, Phys. Rev. Lett. **79**, 2438 (1997).
[11] R. Dörner, H. Bräuning, O. Jagutzki, V. Mergel, M. Achler, R. Moshammer, J. M. Feagin, T. Osipov, A. Bräuning-Demian, L. Spielberger *et al.*, Phys. Rev. Lett. **81**, 5776 (1998).
[12] D. P. Seccombe, S. A. Collins, T. J. Reddish, P. Selles, L. Malegat, A. K. Kazansky, and A. Huetz, J. Phys. B **35**, 3767 (2002).
[13] T. Weber, A. Czasch, O. Jagutzki, A. Müller, V. Mergel, A. Kheifets, J. Feagin, E. Rotenberg, G. Meigs, M. H. Prior *et al.*, Phys. Rev. Lett. **92**, 163001 (2004).
[14] T. Weber, A. O. Czasch, O. Jagutzki, A. K. Muller, V. Mergel, A. Kheifets, E. Rotenberg, G. Meigs, M. H. Prior, S. Daveau *et al.*, Nature (London) **431**, 437 (2004).
[15] T. Weber, A. O. Czasch, O. Jagutzki, A. K. Muller, V. Mergel, A. Kheifets, E. Rotenberg, G. Meigs, M. H. Prior, S. Daveau *et al.*, Nature (London) **443**, 1014 (2006).
[16] M. Gisselbrecht, M. Lavollée, A. Huetz, P. Bolognesi, L. Avaldi, D. P. Seccombe, and T. J. Reddish, Phys. Rev. Lett. **96**, 153002 (2006).
[17] T. Weber, L. Foucar, T. Jahnke, M. Schoeffler, L. Schmidt, M. Prior, and R. Doerner, J. Phys. B **50**, 164002 (2017).
[18] J. M. Feagin, J. Phys. B **31**, L729 (1998).
[19] W. Vanroose, F. Martín, T. N. Rescigno, and C. W. McCurdy, Phys. Rev. A **70**, 050703(R) (2004).
[20] A. S. Kheifets, Phys. Rev. A **71**, 022704 (2005).

[21] W. Vanroose, F. Martín, T. N. Rescigno, and C. W. McCurdy, Science **310**, 1787 (2005).

[22] A. S. Kheifets and I. Bray, Phys. Rev. A **72**, 022703 (2005).

[23] W. Vanroose, D. A. Horner, F. Martín, T. N. Rescigno, and C. W. McCurdy, Phys. Rev. A **74**, 052702 (2006).

[24] J. Colgan, M. S. Pindzola, and F. Robicheaux, Phys. Rev. Lett. **98**, 153001 (2007).

[25] I. A. Ivanov and A. S. Kheifets, Phys. Rev. A **85**, 013406 (2012).

[26] X. Guan, K. Bartschat, and B. I. Schneider, Phys. Rev. A **83**, 043403 (2011).

[27] L. Tao, C. W. McCurdy, and T. N. Rescigno, Phys. Rev. A **82**, 023423 (2010).

[28] W.-C. Jiang, L.-Y. Peng, J.-W. Geng, and Q. Gong, Phys. Rev. A **88**, 063408 (2013).

[29] T. N. Rescigno, D. A. Horner, F. L. Yip, and C. W. McCurdy, Phys. Rev. A **72**, 052709 (2005).

[30] F. L. Yip, C. W. McCurdy, and T. N. Rescigno, Phys. Rev. A **78**, 023405 (2008).

[31] F. L. Yip, C. W. McCurdy, and T. N. Rescigno, Phys. Rev. A **90**, 063421 (2014).

[32] P. G. Burke, *R-Matrix Theory of Atomic Collisions* (Springer, Berlin, 2011).

[33] C. W. McCurdy, M. Baertschy, and T. N. Rescigno, J. Phys. B **37**, R137 (2004).

[34] F. L. Yip, T. N. Rescigno, and C. W. McCurdy, Phys. Rev. A **94**, 063414 (2016).

[35] L. Greenman, R. R. Lucchese, and C. W. McCurdy, Phys. Rev. A **96**, 052706 (2017).

[36] V. I. Lebedev and D. N. Laikov, Dokl. Math. **59**, 477 (1999).

[37] T. N. Rescigno and C. W. McCurdy, Phys. Rev. A **62**, 032706 (2000).

[38] M. E. Rose, *Elementary Theory of Angular Momentum* (Wiley, New York, 1957).

[39] F. L. Yip, C. W. McCurdy, and T. N. Rescigno, Phys. Rev. A **81**, 053407 (2010).

[40] F. L. Yip, F. Martín, C. W. McCurdy, and T. N. Rescigno, Phys. Rev. A **84**, 053417 (2011).

[41] F. Yip, A. Palacios, T. Rescigno, C. McCurdy, and F. Martín, Chem. Phys. **414**, 112 (2013).

[42] F. L. Yip, T. N. Rescigno, C. W. McCurdy, and F. Martín, Phys. Rev. Lett. **110**, 173001 (2013).

[43] S. Huzinaga, J. Chem. Phys. **42**, 1293 (1965).

[44] F. Maulbetsch and J. S. Briggs, J. Phys. B **28**, 551 (1995).